

1 Article

2

Complex Precipitates of TiN-MC_x in GCr15 Bearing 3 Steel

4 **Qianren Tian¹, Guocheng Wang^{1,2,3,*}, Xinghu Yuan¹, Qi Wang^{1,2} and Seetharaman Sridhar³**5 1. School of Materials and Metallurgy, University of Science and Technology Liaoning, Anshan, Liaoning,
6 114051 P. R China.7 2. Key Laboratory of Chemical Metallurgy Engineering Liaoning Province, University of Science and
8 Technology Liaoning, Anshan, Liaoning, 114051 P. R China.9 3. Department of Metallurgical and Materials Engineering, Colorado school of mines, Golden, CO, 80401
10 USA.11 * Correspondence: GUOCHENG WANG, Email Address: wang_guocheng@163.com

12

13 **Abstract:** Nitride and carbide are the second phases which play an important role in the
14 performance of bearing steel, and their precipitation behavior is complicated. In this study, TiN-
15 MC_x precipitations in GCr15 bearing steels were obtained by non-aqueous electrolysis, and their
16 precipitation mechanisms were studied. TiN is the effective heterogeneous nucleation site for Fe₇C₃
17 and Fe₃C, therefore, MC_x can precipitate on the surface of TiN easily, its chemistry component
18 consists of M₃C and M₇C₃ (M = Fe, Cr, Mn) and Cr₃C₂. TiN-MC_x with high TiN volume fraction, TiN
19 forms in early stage of solidification, and MC_x precipitates on TiN surface after TiN engulfed by the
20 solidification advancing front. TiN-MC_x with low TiN volume fraction, TiN and MC_x form in late
21 stage of solidification, TiN can not grow sufficiently and is covered by a large number of precipitated
22 MC_x particles.23 **Keywords:** Non-aqueous electrolysis; TiN-MC_x; Precipitation; Bearings; High carbon chromium
24 bearing steel

25

26

1. Introduction

27 Controlling microstructures and second phase in steel plays an vital role in the quality of steel.
28 Carbide (M₃C, M₃C₂, M₇C₃, M = Fe, Cr, Mn)[1,2] and TiN inclusion[3,4] are common second phase in
29 high carbon chromium steel. Due to the good wear resistance and solid solubility with alloy elements
30 (Cr, Mn)[5,6], carbide can keep good mechanical properties of bearing steel during heat
31 treatment[7,8]. In recent years, utilization of inclusions has become attractive to improve steel
32 performance. TiN is more harmful to bearing steel than Al₂O₃ in the same size[9]. Many studies have
33 investigated TiN and Al₂O₃, MgAl₂O₄ and MnS, and NbC complex precipitation with inclusion[10-
34 13]. Our previous study[14] found that TiN inclusion were covered by carbide in the etched GCr15
35 bearing steel metallographic specimens. Considering the two-dimensional (2-D) of particles cannot
36 reflect their real morphologies, it is necessary to observe their three-dimensional (3-D) morphologies
37 in steel.38 The non-aqueous electrolysis extraction of second phase from steel is an effective method to
39 study their 3-D morphologies and composite interfaces. Fang et al.[15] studied the behaviors of rare
40 earth dissolved in α -Fe, Fe-Ce intermetallic compounds and rare earth inclusions via non-aqueous

41 electrolysis. Bi et al.[16] analyzed 3-D morphology, quantity and chemistry of inclusion in ferroalloys
 42 by the electrolysis method. Wang et al.[17] observed $\text{Al}_2\text{O}_3\text{-MnO-SiO}_2\text{(-MnS)}$ inclusion in steel by
 43 non-aqueous electrolysis. X. W. Zhang et al.[18,19] analyzed Ca-Mg spinel in cord steel and MnS in
 44 heavy rail steel by the electrolysis. D. Zhang et al.[20] studied the suitable electrolytic conditions for
 45 16MnCr5 steel.

46 In this study, 3-D morphologies of the carbide (MC_x , M = Fe, Cr, Mn) and TiN- MC_x precipitates
 47 extracted from GCr15 bearing steel specimens by the non-aqueous electrolysis were observed by field
 48 emission scanning electron microscope - energy dispersive spectrometer (FESEM - EDS). The MC_x
 49 chemistry component was confirmed by X-ray diffraction (XRD) and FactSageTM phase diagram
 50 calculation. The precipitation mechanism of TiN- MC_x with different volume fraction in GCr15
 51 bearing steels was elucidated.

52 2. Experimental

53 2.1. Chemical Components Analysis

54 The chemical compositions of GCr15 bearing steel produced by the basic oxygen furnace (BOF)-
 55 laddle furnace (LF)-vacuum degas (VD)-continuous casting (CC) process in a foundry were
 56 determined by direct-reading spectrometer (Model: ARL-3460 Optical Emission Spectrometer,
 57 Thermo Fisher Corporation). The total oxygen and total nitrogen contents were analyzed using a
 58 nitrogen-oxygen analyzer (Model: TC-600, LECO Corporation). The chemical compositions of the
 59 GCr15 bearing steel are shown in **Table 1**.

60 **Table 1.** Chemical Compositions of GCr15 Bearing Steel (in mass percent).

Composition	C	Si	Mn	P	S	Ti	Cr	V	N	Alt	Ca	O(T)
Concentration	1.01	0.25	0.36	0.012	0.0014	0.0078	1.46	0.0099	0.0049	0.012	<0.005	0.0009

61 2.2. Non-aqueous electrolysis and XRD detection

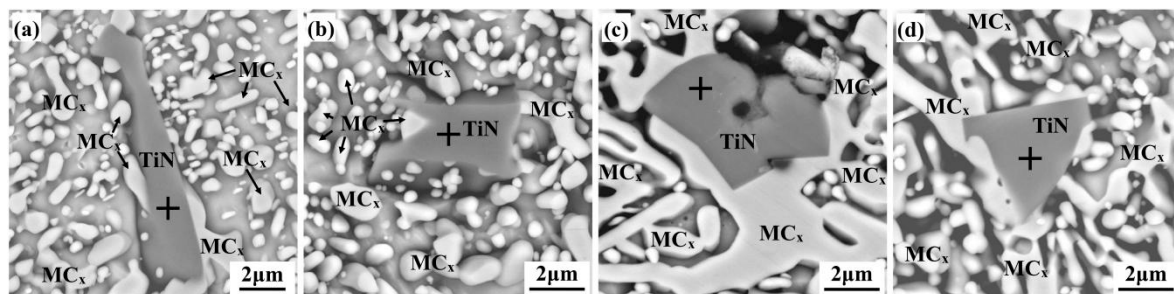
62 The non-aqueous electrolysis method was used to extract TiN- MC_x particles from the GCr15
 63 bearing steel. Samples with diameter of 10 mm and height of 100 mm were as anode and copper as
 64 cathode. The electrolyte consists of 1% tetramethylammonium chloride, 5% triethanolamine, 5%
 65 glycerol, and 89% anhydrous methanol (in volume percentage). The constant voltage DC power
 66 supply (model: DH1720A-1) was used to keep the current density between 40 - 60 mA/cm². The
 67 temperature of the electrolyte was kept at 268 - 278 K (- 5 - 5 °C). Argon gas was used to stir organic
 68 electrolyte. After electrolysis, steel samples were placed to a beaker containing ethanol and vibrated
 69 with ultrasonic wave to separate all particles from the samples surface. MC_x and inclusions in ethanol
 70 were further separated by the magnetism. The inclusion particles were transferred directly to the
 71 double-sided carbon bands attached to the conductive material, and then were observed by FESEM-
 72 EDS. After magnetic separation, MC_x was analyzed by XRD (Model: X'Pert Powder, Malvern
 73 PANalytic Ltd. the detection parameters are that $\text{Cu K}\alpha\lambda = 0.154178$ nm, tube current 40 mA and tube
 74 voltage 40 kV, scanning scope 30 - 85°, step length 0.013 s, residence time 5 s).

75 3. Result

76 3.1. Observation for Particles

77 2-D morphologies of TiN- MC_x in the metallographic specimens etched by 4% nitric acid alcohol
 78 are observed by FESEM-EDS and shown in **Figure 1**. The EDS points are the black crosses and the
 79 analysis for elements can be seen both in **Figure 1**. The dark grey particles are TiN inclusions, and the
 80 light grey particles are MC_x . **Figure 1(a)** shows a long strip and large size TiN with a small amount

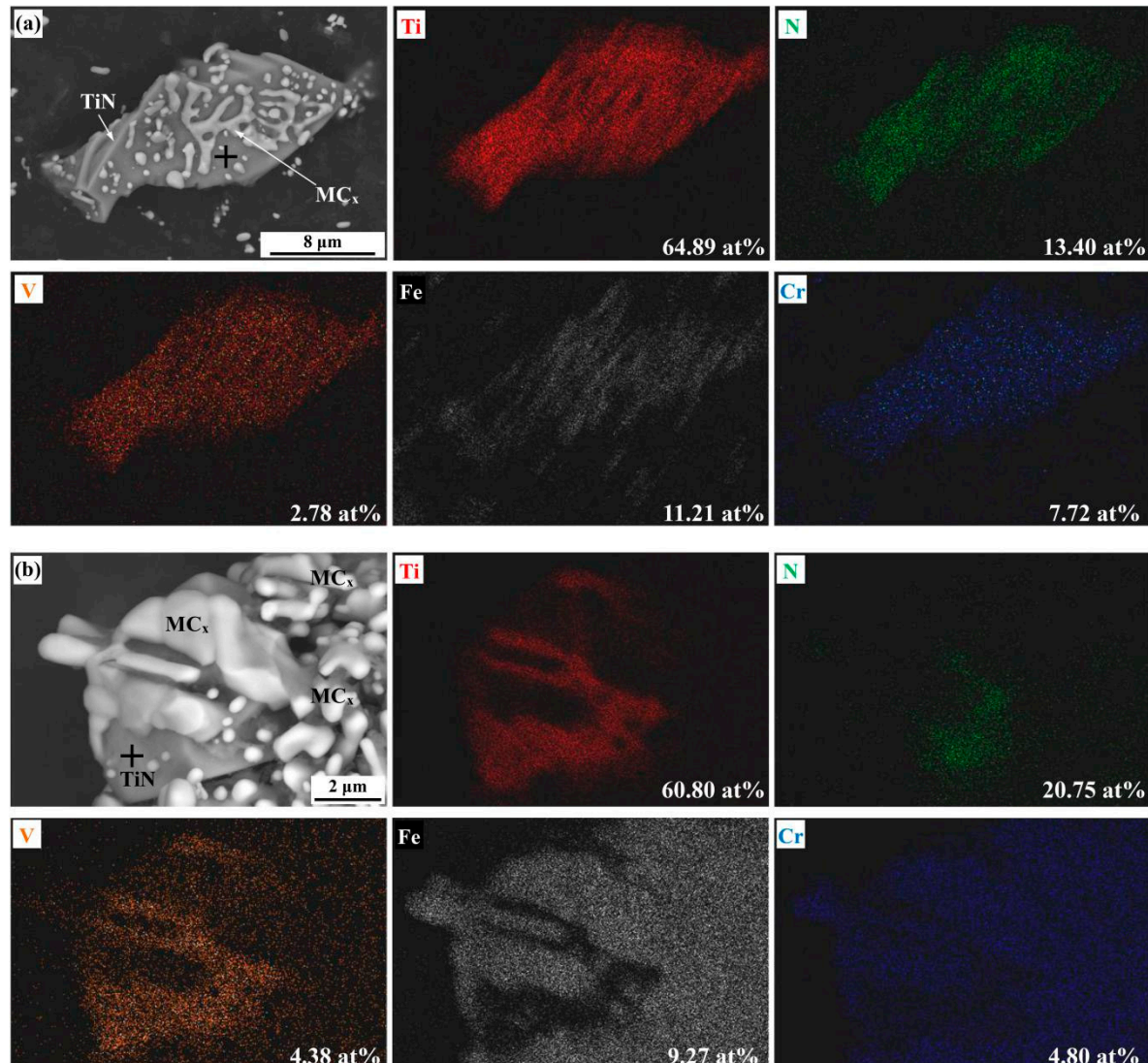
81 of MC_x around it. **Figures 1(b) to (d)** show TiN with less pronounced aspect ratios and its covered by
 82 a larger number of MC_x , which in some cases form a continuous layer rather than discrete particles.



No.	EDS point analysis (element in atomic percentage)				
	Ti	N	V	Cr	Fe
(a)	54.78	34.91	2.65	6.20	1.46
(b)	53.89	41.05	1.27	2.36	1.42
(c)	40.28	44.95	2.45	7.56	4.12
(d)	46.09	46.02	2.43	4.12	1.34

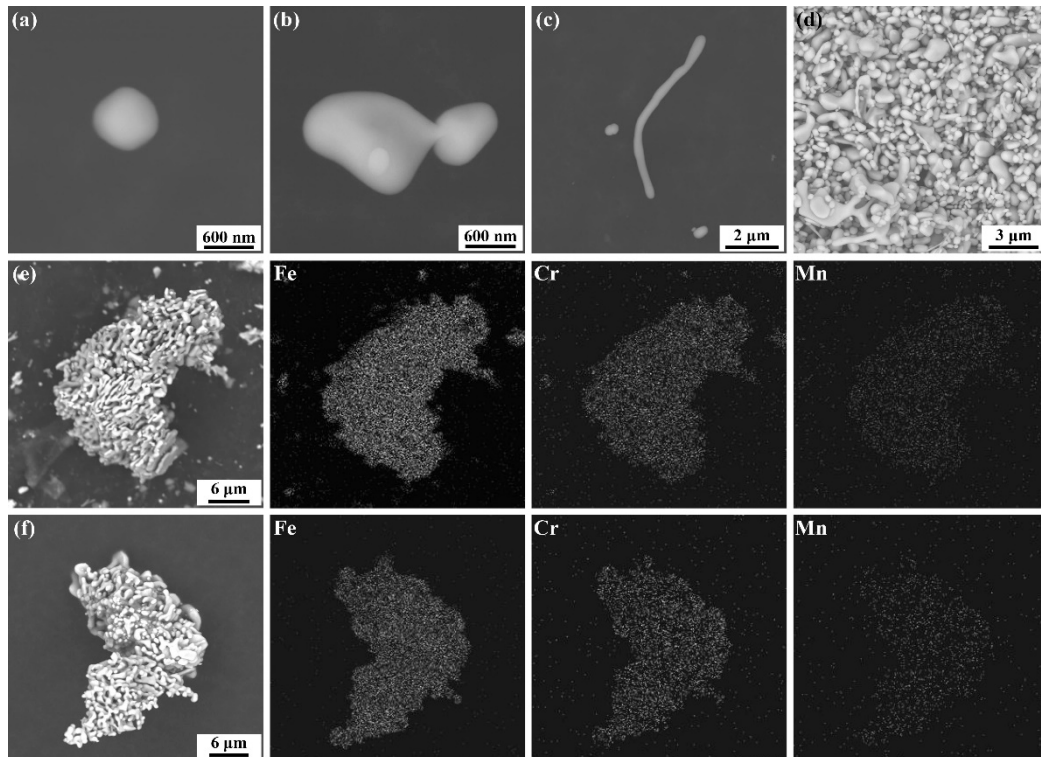
83
 84 **Figure 1.** TiN- MC_x particles and EDS point analysis for TiN part in etched metallographic specimens.
 85 (a) long-strip and large size TiN with MC_x ; (b) - (d) small size TiN with MC_x .

86 3-D morphologies, chemistries of TiN- MC_x and EDS point analysis for TiN part were also
 87 observed by FESEM-EDS, the atomic percentage of element can be seen in each element mapping.
 88 **Figure 2(a)** shows TiN- MC_x with large size TiN inclusion (in comparison to MC_x) whose size is
 89 approximately 25 μm . This category of TiN- MC_x is denoted as “TiN- MC_x with high TiN volume
 90 fraction” in this paper. The elements mapping shows that Ti and V can form the solid solution, while
 91 the metallic elements in MC_x are Fe and Cr, Mn can not be detected because of its low content. **Figure**
 92 2(b) shows that TiN- MC_x with small size TiN are approximately 5 μm , its shape is closer to a sphere.
 93 Compared with the TiN- MC_x in **Figures 2(a)**, TiN in the precipitates is clearly smaller. This category
 94 of TiN- MC_x is denoted as “TiN- MC_x with low TiN volume fraction”. The TiN- MC_x with low TiN
 95 volume fraction is almost completely covered by MC_x .



97 **Figure 2.** Morphologies and elements mapping of TiN-MCx and EDS point analysis for TiN part. (a)
98 high TiN volume fraction; (b) low TiN volume fraction.

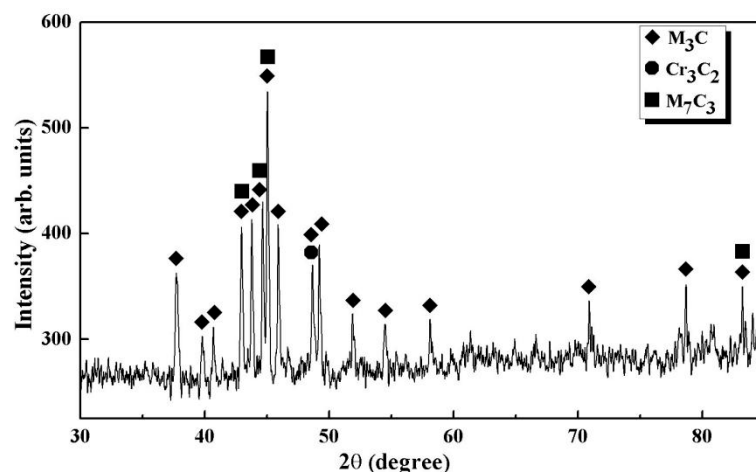
99 **Figure 3** shows the 3-D morphologies of MC_x and elements mapping of Fe, Cr, and Mn. The
100 morphologies of single MC_x particles are not significantly different from that of MC_x on the surface
101 of TiN inclusion. **Figure 3(a)** shows a spherical MC_x with a smaller size less 1 μm. **Figure 3(b)** shows
102 a flat MC_x with approximate 1 μm whereas a MC_x with a shape of a long strip of length 6 μm in
103 **Figure 3(c)**, which is rarely found in steel. **Figure 3(d)** shows MC_x transferred on the conductive
104 carrier, and the MC_x are predominantly spherical and flat. **Figures 3(e) and (f)** are cluster-like MC_x
105 with Fe, Cr and Mn elements mapping results. The size of cluster-like MC_x are approximately 15 μm.
106 However, the cluster-like MC_x exhibits the morphology of banded or reticulated MC_x in
107 metallographic samples. In **Figures 3(e) and (f)**, C is not shown since MC_x and inclusions were
108 transferred on the carbon bands.



109
110 **Figure 3.** Morphologies and elements mapping of MC_x . (a) ball-like MC_x ; (b) flat-like MC_x ; (c) long
111 stripe-like; (d) MC_x transferred on the conductive carrier; (e) and (f) cluster-like MC_x with elements
112 mapping of Fe, Cr, and Mn.

113 3.2. XRD Result

114 **Figure 4** shows the result of MC_x XRD experiment, the structure of MC_x are predominantly M_3C
115 and M_7C_3 , with M_3C being the dominant carbide. At $2\theta = 48.6^\circ$, there are a few Cr_3C_2 . The results are
116 similar to carbides in GCr15 bearing steel after electroslag remelting-continuous casting (ESR-CC)
117 process by Du et al.[2] The main MC_x in that study were M_3C , M_3C_2 and M_7C_3 , and the content of Cr
118 in their sample was 1.47% and 0.31%[2], respectively, which is similar to that in our steel.

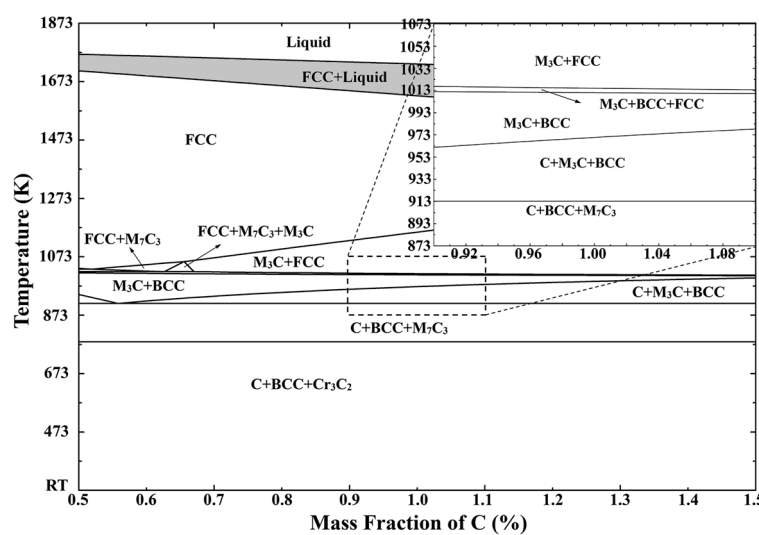


119
120 **Figure 4.** XRD analysis result of the extracted MC_x in the GCr15 bearing steel.

122 4. Discussion

123 4.1. Thermodynamic Analysis

124 The phase diagram of Fe-1.5%Cr-C system was calculated by using the FactSageTM 7.2
 125 thermodynamic software and steel database[21]. The calculated phase diagram for the conditions,
 126 [pct Cr] = 1.5, [pct C] = 0.5 - 1.5 ([pct element] is mass percent of the element in steel), and the
 127 temperature range from 298 K (25 °C) to 1873 K (1600 °C), is shown in **Figure 5** and the gray part
 128 presents the mushy zone of steel. When [pct C] = 1, equilibrium transformation of steel is that liquid
 129 → FCC + liquid → FCC → M₃C + FCC → M₃C + FCC + BCC → M₃C + BCC → C + M₃C + BCC → C +
 130 BCC + M₇C₃ → C + BCC + Cr₃C₂. The liquidus temperature and solidus temperature are close to the
 131 calculated values in our previous paper [liquidus and solidus temperature are 1723 K (1450 °C) and
 132 1601 K (1328 °C), respectively][14]. When the temperature is slightly lower than 1173 K (900 °C), M₃C
 133 gradually precipitates from FCC phase; when the temperature is approximately 913 K (640 °C), M₃C
 134 gradually transforms to M₇C₃; and when the temperature is slightly higher than 773 K (500 °C), the
 135 carbide gradually transforms into Cr₃C₂. In the actual process, phase transformation will be difficult
 136 to be completed to the phase fraction dictated by the equilibrium phase diagram which leads to the
 137 transition layers. The main phases formed during temperature gradual decreasing are M₃C, M₇C₃,
 138 Cr₃C₂, and their content decreases in turn. FactSageTM calculation results are consistent with XRD
 139 result, in which MC_x are found to be M₃C, M₇C₃ and Cr₃C₂.



140

141 **Figure 5.** Phase diagram for Fe-1.5%Cr-C system (the shadow part is the mushy zone of steel, C
 142 presents the pure substance C(s); M₃C (Cementite) presents Fe₃C with dissolved Cr, Mn; M₇C₃
 143 presents carbide phase found in Cr, Mn-containing steels; FCC and BCC present the face-centered
 144 cubic iron (γ -Fe) and body-centered cubic iron (α -Fe), respectively).

145 According to the authors previous work[14,22], TiN precipitates in the mushy zone of GCr15
 146 bearing steel, and their size is affected by the concentration of Ti and N around TiN crystal nucleus.
 147 Ti and N both are positive segregation elements ($k > 0$), their concentrations and consequently the
 148 supersaturation increases with solid fraction increasing, and TiN precipitation become easier during
 149 solidification process. Recently, Li et al.[23] studied the precipitation of TiN inclusions in GCr15
 150 bearing steel during solidification by calculating the thermodynamics and growth kinetics
 151 considering solidification segregation of the solute elements, they believe that the effect of Ti content
 152 on the size of TiN inclusions is greater than that of N content.

153 Fe, Cr, Mn, and C can precipitate on TiN, which is the heterogeneous nucleation site for MC_x. It
 154 is seen in **Figure 2(a)** that the size of TiN is large and consequently, TiN would be formed at the early

155 stage of solidification, and has enough time to growth. TiN in **Figure 2(b)** precipitates at the late stage
 156 of solidification. The diffusion coefficients D_i , $i = \text{Cr, Ti, Mn, C, N}$ in γ -phase were calculated
 157 according to the phase diagrams, when $[\text{pct C}] = 1$ and FCC precipitates at 1673 K (1400 °C). The
 158 relationship between diffusion coefficients and temperature from 1673 to 1173 K (1400 to 900 °C) is
 159 shown in **Figure 6(a)**, and the parameters are shown in **Table 2**. From **Figure 6(a)**, in 1673 - 1642 K
 160 (1400 - 1369 °C), $D_N^\gamma > D_C^\gamma > D_{\text{Ti}}^\gamma > D_{\text{Mn}}^\gamma > D_{\text{Cr}}^\gamma$; in 1642 - 1173 K (1369 - 900 °C), $D_C^\gamma > D_N^\gamma > D_{\text{Ti}}^\gamma > D_{\text{Mn}}^\gamma >$
 161 D_{Cr}^γ . The results indicate that the diffusion of C and N plays a dominant role, the diffusion of C is
 162 more efficient than N after the temperature decreased under 1642 K, while the diffusion of Cr, Ti, and
 163 Mn are extremely small in γ -phase, the content of Cr is much larger than that of Mn and Ti, this
 164 would not affect the precipitation of MC_x . That means that TiN may precipitate more easily in the
 165 range of temperature of 1673 K- 1642 K, while MC_x precipitates easily during the following decreasing
 166 temperature process.

167 **Table 2.** Diffusion Coefficient and Equilibrium Partition Coefficient of C, Cr, Mn, Ti, and N in γ -phase
 168 [24~27].

Element	Equilibrium Partition Coefficient, k	Diffusion Coefficient in γ -phase (cm ² /s)
C	0.34	$0.0761 \cdot \text{EXP}(-134600/RT)$
Cr	0.85	$0.0012 \cdot \text{EXP}(-219000/RT)$
Mn	0.78	$0.486 \cdot \text{EXP}(-276100/RT)$
Ti	0.33	$0.15 \cdot \text{EXP}(-251000/RT)$
N	0.48	$0.91 \cdot \text{EXP}(-168500/RT)$

169 The segregation degree of C, Cr, Ti, Mn, and N during solidification is calculated according to
 170 Equations (1) to (5)[28], in **Figure 6(b)**, at cooling rate of 0.5 K/s, temperature of 1723 K to 1601 K (1450
 171 °C to 1328 °C), corresponding solid fraction is 0~1. The order of segregation from high to low is Ti, C,
 172 N, Mn and Cr at the same solid fraction. The segregation degree of C at the late stage of solidification
 173 reaches tens of times of the initial content. Therefore, MC_x precipitation on the TiN surface becomes
 174 easier at the late stages of solidification.

$$\frac{[\text{pct X}]_t}{[\text{pct X}]_0} = \left[1 - \left(1 - \frac{\beta k_i}{1 + \beta} \right) \cdot f_s \right]^{\frac{k_i - 1}{1 - \frac{\beta k_i}{1 + \beta}}} \quad (1)$$

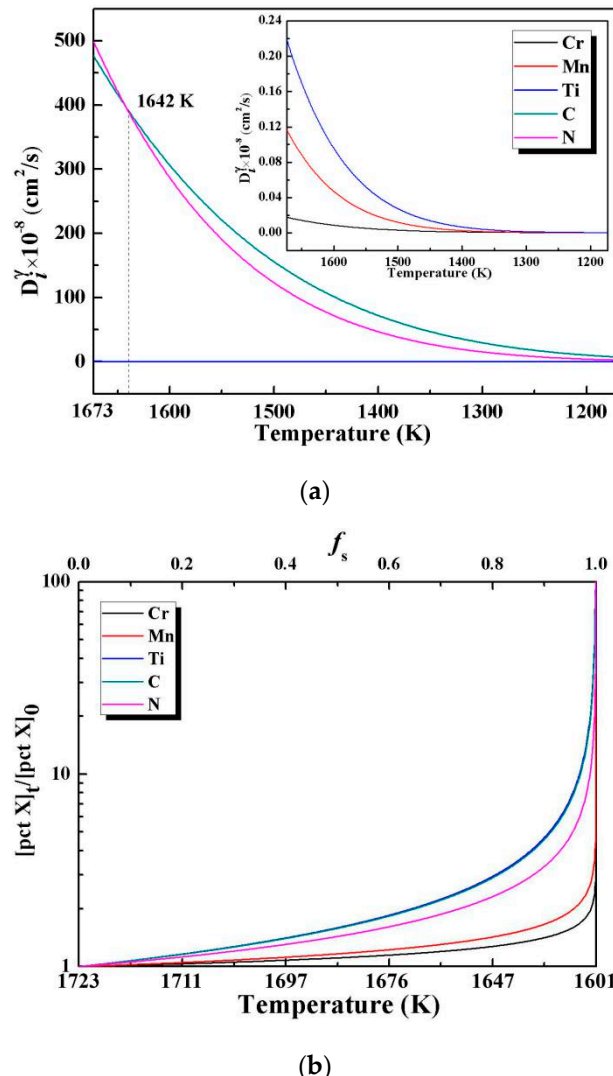
$$\beta = \frac{4D_i^\gamma}{L^2} \quad (2)$$

$$\tau = \frac{T_l - T_s}{R_c} \quad (3)$$

$$L = 143.9 \times R_c^{-0.386}, \quad ([\text{pct C}] = 1) \quad (4)$$

$$T = T_{\text{Fe}} - \frac{T_{\text{Fe}} - T_l}{1 - f_s \frac{T_l - T_s}{T_{\text{Fe}} - T_s}} \quad (5)$$

175 Here, $[pct X]_t$ is the C concentration at solidification front, $[pct X]_0$ is the initial C concentration;
 176 f_s is solid fraction; k_i is equilibrium distribution coefficient of C, Cr, Mn, Ti, and N in γ -phase; D_i^γ is
 177 diffusion coefficient of C, Cr, Mn, Ti, and N in γ -phase, cm^2/s ; τ is the local cooling time, s; R_c is the
 178 local cooling rate, K/s ; L is secondary arm space, μm ; T_{Fe} , T_i , and T_s are the melting point of pure iron
 179 [1809 K (1536 °C)], the liquidus temperature [1723 K (1450 °C)] and the solidus temperature [1601 K
 180 (1328 °C)] of GCr15 steel[14], respectively.



181 **Figure 6.** Diffusion coefficient change in γ -phase and segregation degree of C, Mn, Ti, C, N during
 182 solidification process (a) diffusion coefficient change; (b) segregation degree.

183 *4.2. Crystallographic Analysis*

184 Based on the disregistry theory[29,30], the inconsistency of lattice parameters between matrix
 185 and nucleating phase can indicate the effectiveness of nucleating catalysts. Choosing three crystal
 186 planes and three crystal orientations of the matrix and new phase crystal, the corresponding crystal
 187 parameters can calculate the disregistry between two phases by Equation (6). Since M_3C and M_7C_3
 188 are substitutional solid solutions (Cr and Mn take the position of Fe in carbides)[31], the minimum
 189 disregistry of $TiN-M_3C_3$, $TiN-M_3C$, and $Fe_3C-Fe_7C_3$ were verified by the parameters of TiN [14],
 190 Fe_7C_3 [32] and Fe_3C [33]. The parameters and calculated results are shown in **Table 3**, and the
 191 disregistry diagram is shown in **Figure 7**. The disregistry between $[\bar{1}11](110)TiN \parallel [\bar{1}11](110)Fe_7C_3$,
 192 $[\bar{1}11](110)TiN \parallel [\bar{1}11](110)Fe_3C$ and $[011](100)Fe_3C \parallel [011](100)Fe_7C_3$ are 1.49%, 5.16% and 7.40%,

193 respectively. The results show that the disregistry between TiN and Fe₇C₃ and Fe₃C are both small,
194 and consequently TiN would provide suitable heterogeneous nucleation sites for Fe₇C₃ and Fe₃C.

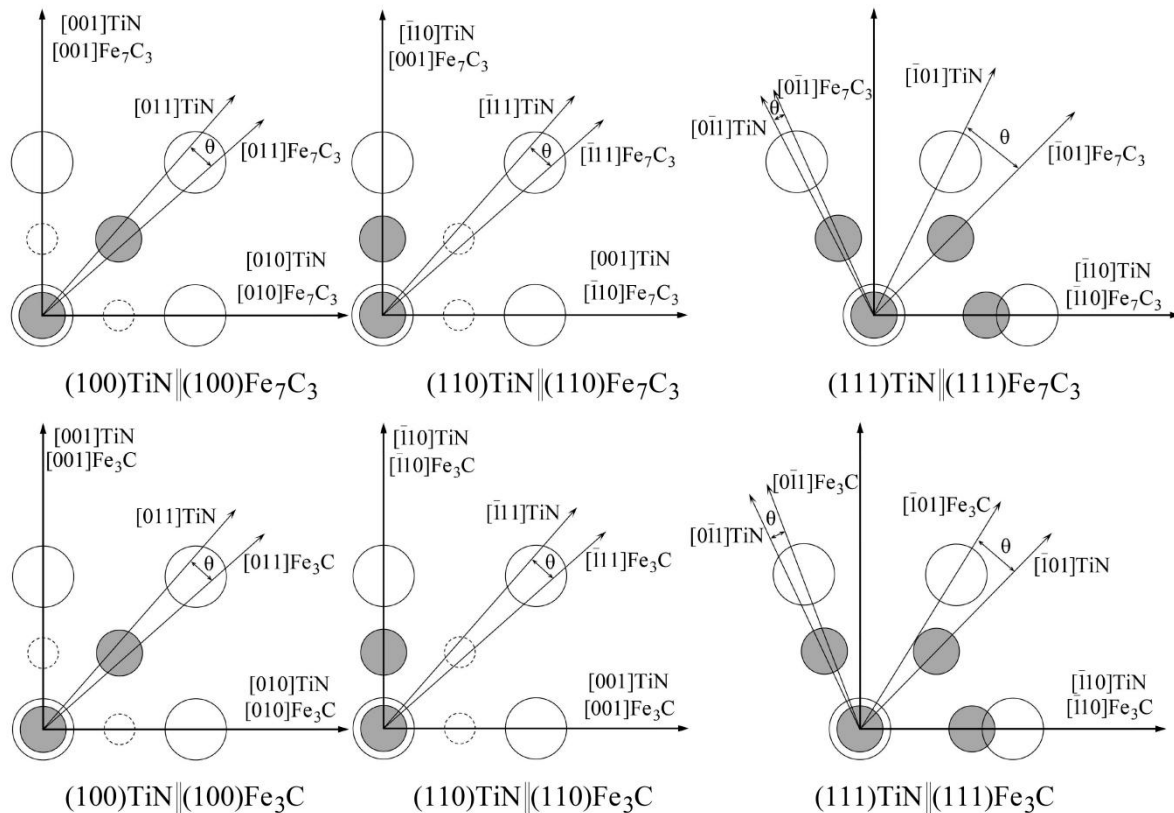
$$\delta_{(hkl)_n}^{(hkl)_s} = \frac{1}{3} \sum_{i=1}^3 \frac{|(d_{[uvw]_s^i} \cdot \cos \theta) - d_{[uvw]_n^i}|}{d_{[uvw]_n^i}} \times 100\% \quad (6)$$

195 where $\delta_{(hkl)_n}^{(hkl)_s}$ is disregistry between a solid plane $(hkl)_s$ and a nucleate plane $(hkl)_n$; $d_{[uvw]_s^i}$ and $d_{[uvw]_n^i}$
196 are the interatomic spacing along a low-index direction $[uvw]_s$ and the interatomic spacing along a
197 low-index direction $[uvw]_n$; θ is the angle between $[uvw]_s$ and $[uvw]_n$.

198 **Table 3.** Parameters and Lattice Disregistry between TiN and Nucleation Phase.

Substance (space group)	Lattice parameters (length unit: Å)					
Fe ₇ C ₃ (Pnma) ^[32]	a	b	C	$\alpha=\beta=\gamma(^\circ)$		
	4.537	6.892	11.913	90		
TiN-Fe ₇ C ₃	[hkl] _s	[hkl] _n	$d_{[hkl]_s}$	$d_{[hkl]_n}$	$\theta(^\circ)$	
	[001]	[001]	2.118	11.913	0(-)	
(100)TiN (100)Fe ₇ C ₃	[011]	[011]	2.995	13.763	14.949	6.52%
	[010]	[010]	2.118	6.892	-	
	[110]	[001]	2.995	11.913	-	
(110)TiN (110)Fe ₇ C ₃	[111]	[111]	3.668	14.492	0.556	1.49%
	[001]	[110]	2.118	8.251	-	
	[011]	[011]	2.995	13.763	5.275	
(111)TiN (111)Fe ₇ C ₃	[101]	[101]	2.995	12.748	18.715	8.93%
	[110]	[110]	2.995	8.251	-	
Substance (space group)	Lattice parameters (length unit: Å)					
Fe ₃ C (Pnma) ^[33]	a	b	C	$\alpha=\beta=\gamma(^\circ)$		
	5.092	6.741	4.527	90		
TiN-Fe ₃ C	[hkl] _s	[hkl] _n	$d_{[hkl]_s}$	$d_{[hkl]_n}$	$\theta(^\circ)$	
	[001]	[001]	2.118	4.527	-	
(100)TiN (100)Fe ₃ C	[011]	[011]	2.995	8.120	11.116	6.92%
	[010]	[010]	2.118	6.741	-	

	[$\bar{1}10$]	[$\bar{1}10$]	2.995	8.448	-	
(110)TiN (110)Fe ₃ C	[$\bar{1}11$]	[$\bar{1}11$]	3.668	9.585	26.551	5.16%
	[001]	[001]	2.118	4.527	-	
	[0 $\bar{1}1$]	[0 $\bar{1}1$]	2.995	8.448	3.227	
(111)TiN (111)Fe ₃ C	[$\bar{1}01$]	[$\bar{1}01$]	2.995	8.120	8.258	9.25%
	[$\bar{1}10$]	[$\bar{1}10$]	2.955	6.813	-	
<hr/>						
Fe ₃ C-Fe ₇ C ₃	[hkl] _s	[hkl] _n	d _{[hkl]_s}	d _{[hkl]_n}	θ(°)	Disregistry
	[001]	[001]	4.527	11.913	-	
(110)Fe ₃ C (110)Fe ₇ C ₃	[$\bar{1}11$]	[$\bar{1}11$]	9.585	14.492	27.107	11.38%
	[$\bar{1}10$]	[$\bar{1}10$]	8.448	8.251	-	
	[001]	[001]	4.527	11.913	-	
(100)Fe ₃ C (100)Fe ₇ C ₃	[011]	[011]	8.120	13.763	26.068	7.40%
	[010]	[010]	6.741	6.892	-	
	[$\bar{1}01$]	[0 $\bar{1}1$]	8.120	13.763	2.983	
(111)FeC ₃ (111)Fe ₇ C ₃	[0 $\bar{1}1$]	[$\bar{1}01$]	8.448	12.748	15.488	21.0%
	[$\bar{1}10$]	[$\bar{1}10$]	6.813	8.251	-	

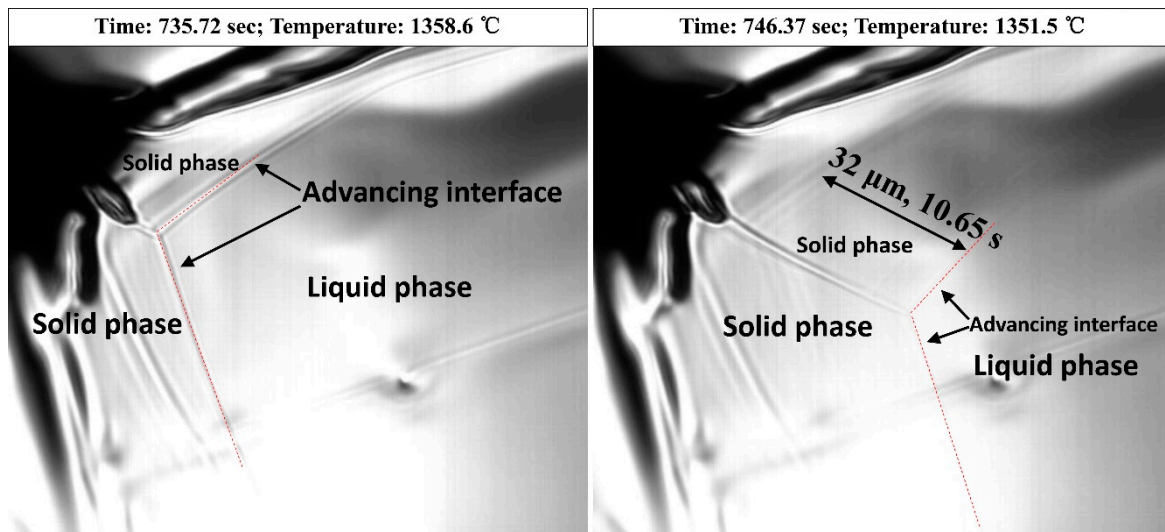


199

200

Figure 7. Schematic diagram of disregistry between TiN and FeCx ($x=3/7, 1/3$).201 *4.3. Pushing and Engulfment Behavior of Particles*

202 Descotes et al.[34] found that TiN particles could be engulfed by the solid side at the solid-liquid
 203 interface in the solidification process. However, Pervushuin et al.[35] reported that TiN was pushed
 204 into the liquid side in molten steel during solidification. In our previous study[22], the local cooling
 205 rate and movement velocity of solidification front are confirmed as 0.7 K/s and 3 $\mu\text{m/s}$ by the
 206 observation of confocal laser scanning microscope (CLSM), respectively. The changes of temperature,
 207 time, and distance are approximately 7 K, 10.6 seconds, and 32 μm , as shown in **Figure 8**. The critical
 208 velocity of pushing or engulfment $V_{\text{cr}}=23/R$ (R is the radius for globular particles)[36], when R comes
 209 to be 12.5 μm and 2.5 μm (the particles in **Figure 2**), V_{cr} are equal to 1.84 $\mu\text{m/s}$ and 9.2 $\mu\text{m/s}$,
 210 respectively. That means the large size TiN inclusion is easier to be engulfed than small size TiN. In
 211 the actual process, the local cooling rate is 0.5 to 10 K/s. The higher the local cooling rate is, the faster
 212 the solidification front moves, and the more easily the inclusions are engulfed.



213

214

Figure 8. Parameters and distance changes of solidification front in GCr15 bearing steel.

215 The size of $\text{TiN}-\text{MC}_x$ is larger than TiN , $\text{TiN}-\text{MC}_x$ moves more slowly than TiN and is easier to
 216 be swallowed by the solidification front. After the engulfment, particles will continue to grow
 217 through solid state diffusion, the rate of which will decrease with decreasing temperature. For $\text{TiN}-$
 218 MC_x pushed to the liquid phase, elements segregation provides possibility for the growth of MC_x on
 219 TiN , $\text{TiN}-\text{MC}_x$ keeps growing until its size is large enough to be engulfed by the solid phase. The
 220 precipitation mechanism of $\text{TiN}-\text{MC}_x$ in different solidification periods can be confirmed.

221 • $\text{TiN}-\text{MC}_x$ with high TiN volume fraction precipitates at the early stage of solidification and has
 222 better growth kinetics in the melt. After being engulfed by the solidification front, MC_x grows at
 223 a lower rate on the surface of TiN .

224 • $\text{TiN}-\text{MC}_x$ with low TiN volume fraction precipitates in the late stage of solidification, and have
 225 no enough time to grow to large size. Due to high C concentration and segregation, a large
 226 amount of MC_x precipitates on TiN surface. When $\text{TiN}-\text{MC}_x$ is large enough and engulfed by the
 227 solidification front, the volume fraction of MC_x is large to cover TiN particle.

228 5. Conclusion

229 In this study, $\text{TiN}-\text{MC}_x$ precipitation mechanism in GCr15 bearing steels were analyzed by
 230 combining the experiments of non-aqueous electrolysis, FESEM observation with EDS, and XRD
 231 analysis, and the theoretical analysis of thermodynamic and crystallographic analysis, and CLSM
 232 observation for pushing and engulfment behavior of particles. The main conclusions can be drawn:

233 (1). $\text{TiN}-\text{MC}_x$ composed of TiN and MC_x , TiN is the effective heterogeneous nucleation site for Fe_7C_3
 234 and Fe_3C , in which the MC_x precipitates on the surface of TiN was observed in GCr15 bearing
 235 steel .

236 (2). MC_x ($\text{M} = \text{Fe, Cr, Mn}$) in GCr15 bearing steel smelted by converter is mainly composed of M_3C ,
 237 M_7C_3 , and Cr_3C_2 .

238 (3). $\text{TiN}-\text{MC}_x$ with high TiN volume fraction precipitates at the early solidification stage. After being
 239 engulfed by the solidification front, MC_x grows at a lower rate on the surface of TiN .

240 (4). $\text{TiN}-\text{MC}_x$ with low TiN volume fraction precipitates in the late solidification stage, and does not
 241 have enough time to grow to large size. When the size of $\text{TiN}-\text{MC}_x$ is large enough and engulfed
 242 by the solidification front, the volume fraction of MC_x is large to cover TiN particle because of
 243 high C concentration and segregation.

244 **Acknowledgments:** The authors gratefully express their appreciation to National Natural Science Foundation
245 of China (Grant Nos. 51874170 and 51634004) for supporting this work.

246 **Conflicts of Interest:** There are no conflicts to declare.

247 **References**

- 248 1. Beswick, J. M.; The effect of chromium in high carbon bearing steels. *Metall. Trans. A* **1987**, *18*, 1897-1906,
249 <https://doi.org/10.1007/BF02647019>.
- 250 2. Du, G.; Li, J.; Wang, Z. B.; Control of carbide precipitation during electroslag remelting-continuous rapid
251 solidification of GCr15 steel. *Metall. Mater. Trans. B* **2017**, *48*, 2873-2890, <https://doi.org/10.1007/s11663-017-1089-3>.
- 253 3. Yang, L.; Cheng, G. G.; Li, S. J.; Zhao, M.; Feng, G. P.; Generation mechanism of TiN inclusion for
254 GCr15SiMn during electroslag remelting process. *ISIJ Int.* **2015**, *55*, 1901-1905,
255 <https://doi.org/10.2355/isijinternational.ISIJINT-2015-253>.
- 256 4. Zhou, D. G.; Fu, J.; Chen, X. C.; Li, J.; Precipitation behavior of TiN in bearing steel. *J. Mater. Sci. Technol.*
257 **2003**, *19*, 184-186. <https://doi.org/10.3321/j.issn:1005-0302.2003.02.028>.
- 258 5. Benz, R.; Elliott, J. F.; and Chipman, J.; Thermodynamics of the carbides in the system Fe-Cr-C. *Metall. Trans.*
259 **1974**, *5*, 2235-2240. <https://doi.org/10.1007/BF02643938>.
- 260 6. Benz, R.; Elliott, J. F.; and Chipman, J.; Thermodynamics of the solid phases in the system Fe-Mn-C. *Metall.*
261 *Trans.* **1973**, *4*, 1975-1986. <https://doi.org/10.1007/BF02665426>.
- 262 7. Krauss, G.; *Principles of Heat Treatment of Steel*, ASM, Metals Park, OH, **1980**, 222-224.
- 263 8. Monma, K.; Maruta, R.; Yamamoto, T.; Wakikado, Y.; Role of spheroidized carbides on the fatigue life of
264 bearing steel. *Jp. Inst. Metall. J.* **1968**, *32*, 1198-1204. <https://doi.org/10.1007/s12540-012-7002-3>.
- 265 9. Fu, J.; Zhu, J.; Di, L.; Tong, F.; Liu, D.; Wang, Y.; Study on the precipitation behavior of TiN in the
266 microalloyed steels. *Acta Metall. Sin.* **2000**, *36*, 801-804. <https://doi.org/10.3321/j.issn:0412-1961.2000.08.005>.
- 267 10. Lee, M. H.; Park J. H.; Synergistic effect of nitrogen and refractory material on TiN formation and equiaxed
268 grain structure of ferritic stainless steel. *Metall. Mater. Trans. B* **2018**, *49*, 877-893.
269 <https://doi.org/10.1007/s11663-018-1218-7>.
- 270 11. Park, J. S.; Kim, D. H.; Park, J. H.; TEM characterization of a TiN-MgAl₂O₄ epitaxial interface. *J. Alloys Comp.*
271 **2017**, *695*, 476-481. <https://doi.org/10.1016/j.jallcom.2016.11.103>.
- 272 12. Liu, Y.; Zhang, L. F.; Duan, H. J.; Zhang, Y.; Luo, Y.; Conejo, A. N.; Extraction, thermodynamic analysis,
273 and precipitation mechanism of MnS-TiN complex inclusions in low-sulfur steels. *Metall. Mater. Trans. A*
274 **2016**, *47*, 3015-3025. <https://doi.org/10.1007/s11661-016-3463-1>.
- 275 13. Lee, Y.; Cooman, B. C. D.; TiN/NbC compound particle formation during thin slab direct rolling of HSLA
276 steel. *Steel Res. Int.* **2014**, *85*, 1158-1172. <https://doi.org/10.1002/srin.201300280>.
- 277 14. Tian, Q. R.; Wang, G. C.; Shang, D. L.; Lei, H.; Yuan, X. H.; Wang, Q.; Li, J.; Precipitation behaviors of TiN
278 inclusion in GCr15 bearing steel billet. *Metall. Mater. Trans. B* **2018**, *49*, 1149-1164.
279 <https://doi.org/10.1007/s11663-018-1230-y>.
- 280 15. Fang, K. M.; Ni, R. M.; Research on determination of the rare-earth content in metal phases of steel. *Metall.*
281 *Trans. A* **1986**, *17*, 315-323. <https://doi.org/10.1007/BF02643907>.
- 282 16. Bi, Y.; Karasev, A.; Jönsson, P. G.; Three-dimensional investigations of inclusions in ferroalloys. *Steel Res.*
283 *Int.* **2014**, *85*, 659-669. <https://doi.org/10.1002/srin.201300157>.

284 17. Wang, G. C.; Li, S. L.; Ai, X. G.; Zhao, C. M.; Lai, C. B.; Characterization and thermodynamics of Al_2O_3 -
285 MnO-SiO_2 (-MnS) inclusion formation in carbon steel billet. *J. Iron Steel Res. Int.* **2015**, *22*, 566-572.
286 [https://doi.org/10.1016/S1006-706X\(15\)30041-8](https://doi.org/10.1016/S1006-706X(15)30041-8).

287 18. Zhang, X. W.; Zhang, L. F.; Yang, W.; Wang, Y.; Liu, Y.; Dong, Y. C.; Characterization of the three-
288 dimensional morphology and formation mechanism of inclusions in linepipe steels. *Metall. Mater. Trans. B*
289 **2017**, *48*, 701-712. <https://doi.org/10.1007/s11663-016-0833-4>.

290 19. Zhang, X. W.; Zhang, L. F.; Yang, W.; Dong, Y. C.; Characterization of MnS particles in heavy rail steels
291 using different methods. *Steel Res. Int.* **2017**, *88*, 1600080(1-16). <https://doi.org/10.1002/srin.201600080>.

292 20. Zhang, D.; Shen, P.; Xie, J. B.; An, J. M.; Huang, Z. Z.; Fu, J. X.; A method for observing tridimensional
293 morphology of sulfide inclusions by non-aqueous solution electrolytic etching. *J. Iron Steel Res. Int.* **2019**,
294 *26*, 275-284, <https://doi.org/10.1007/s42243-018-0142-z>.

295 21. Andersson, J.; A thermodynamic evaluation of the Fe-Cr-C system. *Metallurgical Transactions A* **1988**, *19*,
296 627-636. <https://doi.org/10.1007/BF02649276>.

297 22. Tian, Q. R.; Wang, G. C.; Shang, D. L.; Lei, H.; Yuan, X. H.; Wang, Q.; Li, J.; In Situ Observation of the
298 Precipitation, Aggregation, and Dissolution Behaviors of TiN Inclusion on the Surface of Liquid GCr15
299 Bearing Steel. *Metall. Mater. Trans. B* **2018**, *49*, 3137-3150. <https://doi.org/10.1007/s11663-018-1411-8>.

300 23. Li, B.; Shi, X.; 1,2, Guo H. J.; Guo, J.; Study on Precipitation and Growth of TiN in GCr15 Bearing Steel
301 during Solidification. *Materials* **2019**, *12*, 1463-1475. <https://doi.org/10.3390/ma12091463>.

302 24. Yang, L.; Cheng, G. G.; Zhao, S. J.; Li, M.; Feng, G. P.; Generation Mechanism of TiN Inclusion for
303 GCr15SiMn during Electroslag Remelting Process. *ISIJ Int.* **2015**, *55*, 1901-1905.
304 <https://doi.org/10.2355/isijinternational.ISIJINT-2015-253>.

305 25. Wang, Y. N.; Yang, J.; Bao, Y. P.; Characteristics of BN Precipitation and Growth During Solidification of
306 BN Free-Machining Steel. *Metall. Mater. Trans. B* **2014**, *45*, 2269-2278. <https://doi.org/10.1007/s11663-014-0146-4>.

308 26. Huang, Y. W.; Long, M. J.; Liu, P.; Chen, D. F.; Chen, H. B.; Gui, L. T.; Liu, T.; Yu, S.; Effects of partition
309 coefficients, diffusion coefficients, and solidification paths on microsegregation in Fe-based multinary
310 alloy. *Metall. Mater. Trans. B* **2017**, *48*, 2504-2515. <https://doi.org/10.1007/s11663-017-1045-2>.

311 27. Miettinen, J.; Thermodynamic-kinetic simulation of constrained dendrite growth in steels, *Metall. Mater.*
312 *Trans. B*, **2000**, *31*, 365-379. <https://doi.org/10.1007/s11663-000-0055-6>.

313 28. Ohnaka, I.; Mathematical Analysis of Solute Redistribution during Solidification with Diffusion in Solid
314 Phase. *ISIJ Int.* **1986**, *26*, 1045-1051. <https://doi.org/10.2355/isijinternational1986.26.1045>.

315 29. Turnbull, D.; Vonnegut, B.; Nucleation catalysis. *Ind. Eng. Chem.* **1952**, *44*, 1292-1298.
316 <https://doi.org/10.1021/ie50510a031>.

317 30. Bramfitt, B. L.; The effect of carbide and nitride additions on the heterogeneous nucleation behavior of
318 liquid iron. *Metall. Trans.* **1970**, *1*, 1987-1995. <https://doi.org/10.1007/BF02642799>.

319 31. Ding, M. Y.; Yang, Y.; Wu, B. S.; Li, Y. W.; Wang, T. J.; Ma, L. L.; Study on reduction and carburization
320 behaviors of iron-based Fischer-Tropsch synthesis catalyst. *Energy Procedia* **2014**, *61*, 2267-2270.
321 <https://doi.org/10.1016/j.egypro.2014.12.444>.

322 32. Morniroli, J. P.; Gantois, M.; Etude microstructurale de carbures M7C3. *J. Appl. Crystal.* **1983**, *16*, 1-10.
323 <https://doi.org/10.1107/S0021889883009863>.

324 33. Fruchart, D.; Chaudouet, P.; Fruchart, R.; Rouault, A.; Senateur, J. P.; Etudes structurales de composés de
325 type cémentite: Effet de l'hydrogène sur Fe3C suivi par diffraction neutronique. Spectrométrie Mössbauer
326 sur FeCo 2B et Co 3B dopés au 57Fe. *J. Solid State Chem.* **1984**, *51*, 246-252. [https://doi.org/10.1016/0022-4596\(84\)90340-2](https://doi.org/10.1016/0022-4596(84)90340-2).

328 34. Descotes, V.; Bellot, J. P.; Witzke, S.; Jardy, A.; Modeling the Titanium Nitride (TiN) Germination and
329 Growth during the Solidification of a Maraging Steel. *Proceedings of the 2013 International Symposium on*
330 *Liquid Metal Processing & Casting*, TMS (The Minerals, Metals & Materials Society) 2013, 201-206.
331 https://doi.org/10.1007/978-3-319-48102-9_30.

332 35. Pervushin, G.V.; Suito, H.; Precipitation behavior of TiN in Fe-10mass% Ni alloy during solidification and
333 isothermal holding at 1400 °C, *ISIJ Int.* 2001, 41, 728-737. <https://doi.org/10.2355/isijinternational.41.728>

334 36. Shibata, H.; Yin, H.; Yoshinaga, S.; Emi, T.; Suzuki, M.; In-situ observation of engulfment and pushing of
335 nonmetallic inclusions in steel melt by advancing melt/solid interface. *ISIJ Int.* 1998, 38, 149-156.
336 <https://doi.org/10.2355/isijinternational.38.149>.